A nature-inspired steroid-like electron acceptor to polarity-dependent probe for visualizing lipid evolution in Alzheimer's disease

Lulu Wu[a],†, Wen-Jin Wang[b],†, Yuting Lin[a],†, Weiren Zhong[c], Jifu Wang[c], Jianyu Zhang[d], Zheng Zhao[b], Fritz E. Kühn[e], Yun Xu[f], Qiang Yong[a],*, Ben Zhong Tang[b],*, and Xu-Min Cai[a],[g],*

[a] Jiangsu Co-Innovation Center of Efficient Processing and Utilization of Forest Resources, College of Chemical Engineering, Nanjing Forestry University, Nanjing 210037, China

[b] School of Science and Engineering, Shenzhen Institute of Aggregate Science and Technology, The Chinese University of Hong Kong, Shenzhen (CUHK-Shenzhen), Guangdong 518172, P.R. China

[c] Institute of Chemical Industry of Forest Products, Chinese Academy of Forestry (CAF), Nanjing 210042, China

[d] MOE Key Laboratory of Macromolecular Synthesis and Functionalization, Department of Polymer Science and Engineering, Zhejiang University, Hangzhou 310058, China

[e] Molecular Catalysis, Department of Chemistry & Catalysis Research Center, School of Natural Sciences, Technische Universität München, München D-85747, Germany

[f] Department of Neurology, Nanjing Drum Tower Hospital, Affiliated Hospital of Medical School, Nanjing University, Nanjing 210008, China

[g] Guangdong Provincial Key Laboratory of Luminescence from Molecular Aggregates, Guangzhou 510640, China

***Corresponding authors**
E-mails:
swhx@njfu.com.cn;
tangbenz@cuhk.edu.cn;
xumin.cai@njfu.edu.cn

†Equally contributed to this work

Abstract

To date, most optical materials are derived from petrochemicals, facing problems like renewability, sustainability, and biocompatibility. Fluorescent materials derived from natural products with unique structures, stimuli-responsive photophysical properties, and superior compatibility are of extraordinary significance for biomedical applications. In this work, a nature-inspired electron acceptor with a steroid-like structure (DABT) has been constructed based on the tricyclic diterpene skeleton of natural rosin. Through substitution with variable electron donors, red-shifted and twisted intramolecular charge transfer can be realized. In particular, the dimethyl amino substituted compound, DABT-DMA, can be applied as a polarity-dependent bio-sensor with a dual responsiveness of distinct fluorescence wavelength and lifetime due to its outstanding solvent effect. In addition to the advantageous biocompatibility and steroid-like structure of DABT-DMA, successful lipid droplet-targeted imaging at dual channels can be achieved. Further investigations prove that dysfunction of lipid droplets induced by Aβ protein can result in the accumulation of cholesterol analogs, further exacerbating the pathological features of Alzheimer's disease. This work not only proposes a novel natural electron acceptor with a steroid-like structure possessing both biocompatibility and targeting capability but also offers new insights into Alzheimer's disease-related pathophysiological mechanisms, paving the way toward potential diagnostics.

Introduction

Nature is a huge treasure trove, and the natural products it creates have attracted widespread attention due to their remarkable pharmacological properties[1-3]. Many natural products exhibit multiple pharmacological effects, nevertheless, their specific action modes are often unclear, delaying the development of natural medicines[4]. Fluorescence technology helps to trace the physiological processes of natural medicines in treatment, thus broadening the application prospects in theranostics[5-7]. The earliest natural luminescent material escribed has been considered to be a blue fluorescent secretion from a Mexican wood discovered by Nicolas Monardes in the 16th century[8-

[9]. Over the past five centuries, researchers have gradually paid more interest in natural luminescent products[10-16]. Recently, the exploration of natural fluorescent materials has been accelerated. Due to the many unique natural scaffolds (aromatic rings, heteroatoms, and flexible twisted structures, etc.), natural products such as berberine[17], quercetin[18], tanshinone IIA[19], and coumarin[20] have been found to exhibit aggregation-induced emission (AIE) properties, showing great potential for biomedical applications such as bioimaging and photodynamic therapy. However, the limited variety of AIE materials either extracted from biomass or possessing natural skeletons (BioAIE) as well as the low content of some natural fluorescent products make the development of BioAIE materials rather challenging. Based on our previous experiences, chemical construction of BioAIE materials containing unique natural scaffolds with excellent biocompatibility and renewability is a reasonable strategy and will hold great promise in the biomedical field[21-22].

Rosin, extracted from natural pine resin, is an abundantly renewable resource that contains unique structures based on benzene rings, alicyclic rings, and oxygen atoms. Rosin and its derivatives exhibit good biocompatibility and hold great potential for various biological applications[23-26]. The tricyclic diterpene rosin scaffold can be easily applied to construct tetracyclic steroid analogs. Steroids constitute a distinctive but significant class of lipids in humans, performing a variety of physiological functions. As a key member of steroids, cholesterol is one of the essential lipids for the human body. Due to its structural distinctions compared to other lipids such as fatty acids, phospholipids, and glycolipids, cholesterol is relatively non-polar and therefore hydrophobic, mainly stored in lipid droplets (LDs)[27-29]. However, elevated cholesterol levels are closely related to pathological conditions such as cardiovascular disease and neurodegenerative diseases[30-32]. At present, Alzheimer's disease (AD), the most common neurodegenerative disease among older people, is threatening the health of an increasingly large elderly population worldwide[33-35]. Clinical investigations and epidemiological studies have shown that in addition to amyloid-β plaques in the brain, abnormal lipid metabolism also poses a significant impact on the onset of AD[36-38]. Lipid metabolism abnormalities are usually reflected in changes in the number, size,

distribution, and polarity of LDs[39-41]. While the number, size, and distribution of LDs can be assessed through morphological studies, the detection of the lipid evolution in LDs has not been disclosed so far. Therefore, monitoring the lipid polarity in LDs is of high significance for the clinical diagnosis and treatment of AD.

Fluorescent probes with polarity-sensitive characteristics are typically structured in the form of electron donor-acceptor (D-A) pairs[42]. The regulation of D/A moieties has a significant impact on improving the performance of D-A-typed fluorescent materials. Due to its diversity and ease of modification, the regulation of electron donors has become the dominant design strategy for constructing D-A-typed fluorescent molecules[43-44]. In comparison, the variety of electron acceptors is relatively limited, mainly concentrated on naphthalimide[45], imidazole[46], and benzothiadiazole[47-48], all of which are derived from fossil fuels. Investigation on the natural electron acceptors, however, are rare[22]. If the electron acceptors could be designed based on the natural skeletons, significant innovations in the development of new D-A-typed fluorescent probes might be possible. In short, the development of natural D-A-typed BioAIE probes with polarity sensitivity coupled with excellent biocompatibility is of great significance for achieving dynamic monitoring of lipid metabolism during AD.

Analogous to the tetracyclic structure of cholesterol, a novel natural electron acceptor, dehydroabietic acid-thiazole (DABT), has been designed, derived from the natural tricyclic product of dehydroabietic acid (Figure 1). Further, a series of D-A-typed BioAIE materials based on DABT with variable electron donors (Cz, TPA, and DMA) has been synthesized, exhibiting high sensitivity to the environmental polarity due to the twisted intramolecular charge transfer (TICT) property. Benefiting from its steroid structure and advantageous biocompatibility, DABT-DMA can specifically target LDs. With both bi-channel fluorescence imaging and fluorescence lifetime imaging microscopy (FLIM), it has been found that the polarity of LDs decreases during the AD process. Further investigation suggests that the increased content of cholesterol analogs induced by Aβ protein in LDs may contribute to the observed polarity decrease. This study has not only developed a novel natural electron acceptor but also provides a new bio-based probe for visualizing lipid evolution in LDs during the AD process, offering

fresh insights into potential AD-related pathophysiological mechanisms.

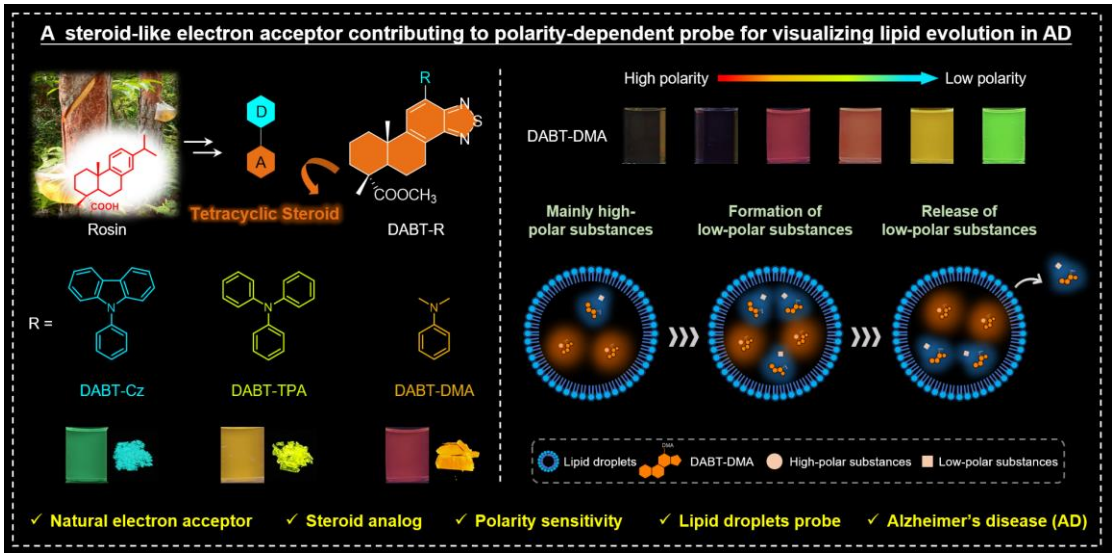

Figure 1. Molecular design of rosin-derived D-A typed polarity-dependent probe in monitoring lipid evolution in LDs during AD.

Results and Discussion

Molecular design

The exploration of novel electron acceptors is of great significance for the construction of D-A-typed molecules. Natural electron acceptors derived from natural products may endow the obtained materials with unique photophysical properties and advantageous biocompatibility. The natural product dehydroabietic acid, extracted from dis-proportionated rosin, can be chemically modified into the precursor DAMBDA[49], which can be converted from the tricyclic structure into a steroid analog, i.e., rosin-based natural electron acceptor DABT, through a cyclization reaction. Due to the presence of Br substituents in the intermediate DABT, various electron donors can be introduced through C-C and C-N coupling. Carbazole (Cz), triphenylamine (TPA), and *N,N*-dimethylamino (DMA) are three typical electron donors with varying degrees of electron-donating ability, which can be used for the construction of D-A molecules of DABT-Cz, DABT-TPA, and DABT-DMA (Scheme 1), achieving regulated photophysical properties. The structures and purities of the obtained products have been confirmed by NMR, HRMS, and single-crystal X-ray diffraction measurements

(Figures S1-S9 and Table S1, Supporting Information).

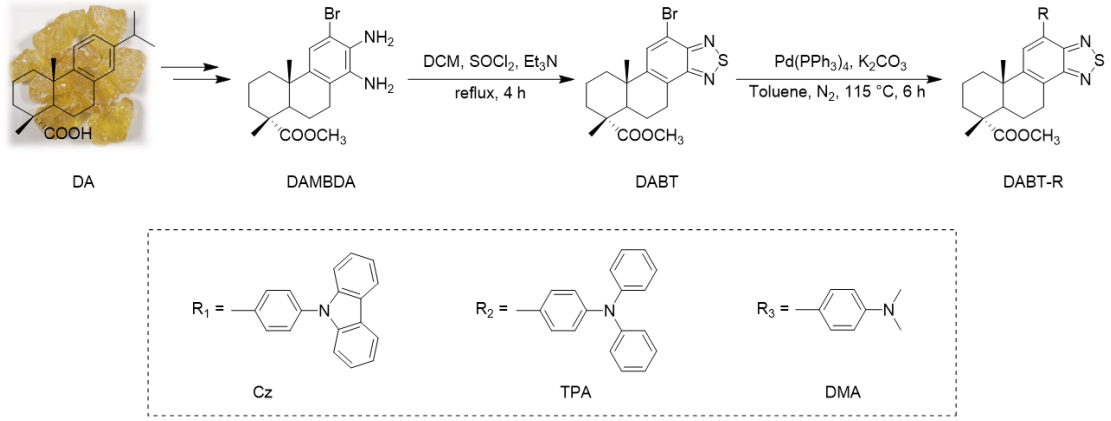

Scheme 1. Synthesis of DABT-Cz, DABT-TPA, and DABT-DMA.

Photophysical properties in the molecular, aggregate, and solid states

The photophysical properties of the above-mentioned natural electron acceptor-based molecules have been studied first. Figure 2a intuitively shows the fluorescence variation of the three molecules in the tetrahydrofuran (THF)/H_2O mixed system with different water factions (f_w). In dilute solutions (f_w = 0%), DABT-Cz, DABT-TPA, and DABT-DMA exhibit a red-shifted trend of fluorescence with green, orange, and red colors, respectively. When f_w increases, each sample initially red-shifts and then blue-shifts, while the fluorescence intensity first decreases and then increases, apparently exhibiting TICT and AIE characteristics. Through absorption and photoluminescence (PL) spectra (Figure 2b), it has been found that the absorption peak of DABT-series molecules red-shifts from 373 (DABT-Cz) to 424 (DABT-DMA) nm, and the corresponding emission has accordingly red-shifts from 505 nm to 607 nm. This is consistent with the increased electron-donating ability from Cz to DMA[50]. The spectral data with different f_w in Figures 2c-e and S10 show corresponding trends for the DABT-series compounds depicted in Figure 2a. At low f_w, due to the increase in solvent polarity, the molecular conformation is distorted to stabilize the separated charge, hence leading to a red-shifted and weakened emission, exhibiting a TICT effect in the isolated state[51]. As f_w increases, the formation of molecular aggregates leads to a decrease in environmental polarity, resulting in a blue-shift in the emission. The restriction of

intramolecular motion in the aggregate state turns on the fluorescence, leading to the AIE characteristics[52]. The TICT-AIE performance of these molecules demonstrates the feasibility of constructing D-A-typed BioAIE materials using DABT as a natural electron acceptor and the luminescence performance can be regulated by adjusting the donating ability of electron donors.

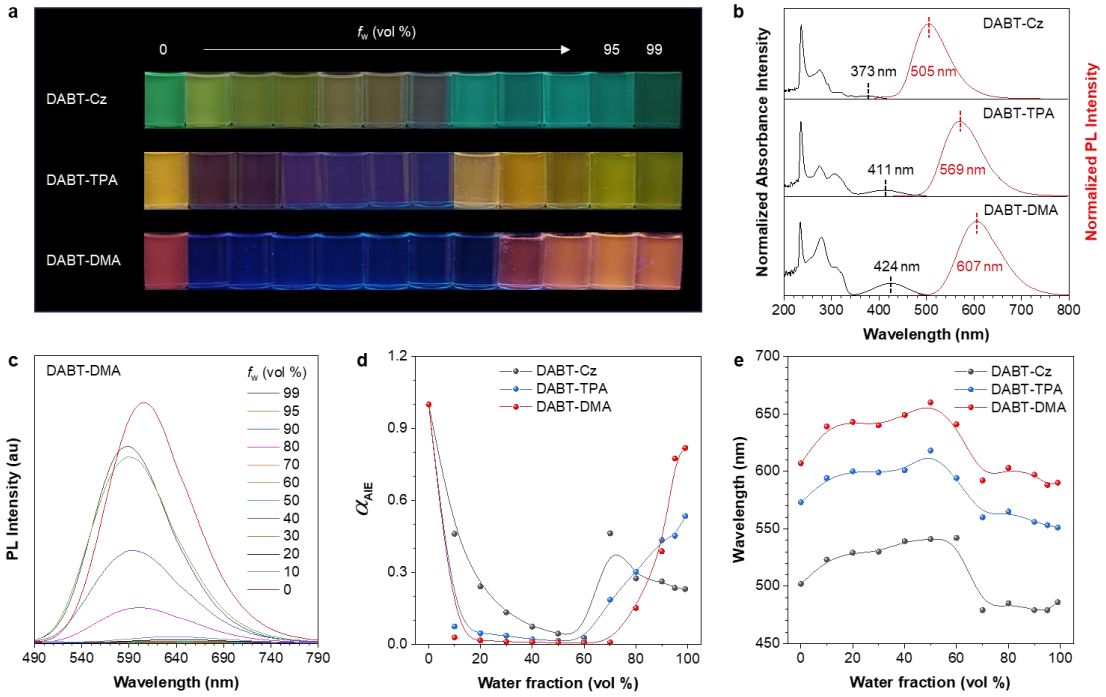

Figure 2. (a) Fluorescence photographs of DABT-Cz, DABT-TPA, and DABT-DMA in THF/H_2O mixtures with different water fractions (f_w) taken under 365 nm UV irradiation. (b) Normalized absorption and PL spectra of DABT-Cz, DABT-TPA, and DABT-DMA in pure THF solutions. (c) PL spectra of DABT-DMA in THF/H_2O mixtures with different f_w. (d-e) The plots of the (d) α_{AIE} and (e) emission maximum versus f_w of DABT-Cz, DABT-TPA, and DABT-DMA. $\alpha_{AIE} = I/I_0$, I_0 = PL intensity in pure THF solution. Concentration: 10 μM; DABT-Cz: λ_{ex} = 373 nm; DABT-Cz: λ_{ex} = 411 nm; DABT-DMA: λ_{ex} = 424 nm.

Based on the TICT-AIE characteristics of the DABT-series molecules mentioned above, we have further investigated the solid-state photophysical properties of these molecules. Similar to both the solution and aggregate states, with the enhancement of electron-donating properties, the emission of solid-state DABT-Cz, DABT-TPA, and

DABT-DMA also exhibits a red-shifted trend from 479 to 571 nm (Figures S11 and S12), indicating that the molecular structure can simultaneously affect the photophysical properties of the solids. Interestingly, DABT-DMA exhibits the highest quantum yield (QY) of 54.5% compared to that of DABT-Cz (18.9%) and DABT-TPA (13.4%). This result contradicts the energy gap law, which suggests that compounds with larger energy gaps to redder emission typically exhibit weaker fluorescence[50, 53]. This may be attributed to the important role played by its aggregate structure of packing. In order to investigate the underlying reasons, single crystals of DABT-TPA and DABT-DMA have been obtained and the crystal-structure analysis has been implemented using single-crystal X-ray diffraction (Figure S12c). The collection and summary of crystal data and specific parameters are presented in Table S1. Regarding the conformation, it can be seen that both DABT-TPA and DABT-DMA have large twisted conformations. DABT-DMA has a larger twist angle ($\theta = 48.62°$) than that of DABT-TPA ($\theta = 28.78°$), which may lead to larger intramolecular charge separation and result in a red-shift in the fluorescence[54]. From the perspective of aggregate structure, DABT-DMA shows stronger intermolecular interactions, providing a rigid environment to inhibit molecular motion, thus suppressing the non-radiative transitions to result in larger QY (Figure S12c). These results indicate that the molecular conformation is more inclined to determine the emission wavelength, while aggregation structures can regulate intermolecular forces, thereby affecting emission intensity. In summary, the combined effect of molecular and aggregate structures synchronically regulates the photophysical properties of fluorescent solids based on the natural electron acceptor skeleton.

Polarity responsiveness of fluorescence wavelength and lifetime

Due to the D-A structure of the DABT-series compounds, the photophysical properties in different organic solvents have been investigated to explore the polarity responsiveness. As shown in Figure 3a-d, it can be visually observed that with increasing of solvent polarity, all molecules exhibit a trend of reduced fluorescence intensity with a red shift in the emission wavelength. The maximum emission wavelength of DABT-Cz red-shifts from 466 (cyclohexane, Cy) to 555 (dimethyl

sulfoxide, DMSO) nm, with a redshift of 89 nm. Both DABT-TPA and DABT-DMA undergo a redshift of 108 and 152 nm, respectively. The maximum emission wavelengths of DABT-Cz, DABT-TPA, and DABT-DMA show a good linear relationship with solvent polarity (Figure 3e), with linear correlation coefficients of 0.99, 0.99, and 0.97, and slopes of 6.51, 7.71, and 10.81, respectively. The Lippert Mataga plot also illustrates solvent effects (Table S2 and Figure S13), with slopes of 11.73, 11.90, and 13.43, respectively. The maximum slopes of DABT-DMA (10.81 of linear correlation coefficient and 13.43 of the Lippert Mataga plot) indicate that its solvent effect is the strongest, suggesting its largest conformational change in different polar solvents. The reason for the distinctions may be that DMA has the strongest electron-donating ability and is more sensitive to changes in the dipole moment, promoting the strongest solvent effect therein. To further investigate the polarity response of DABT-DMA to variable solvents, its fluorescence lifetime in different solvents has been examined. As the polarity increases, the fluorescence lifetime shows an overall decreasing trend, specifically from 10.8 ns in Cy to 1.9 ns in DMSO (Figure 3f). The significant changes in the emission wavelength, as well as the fluorescence lifetime of DABT-DMA in variable polar environments, indicate their potential as fluorescent probes for monitoring polarity changes in biological microenvironments.

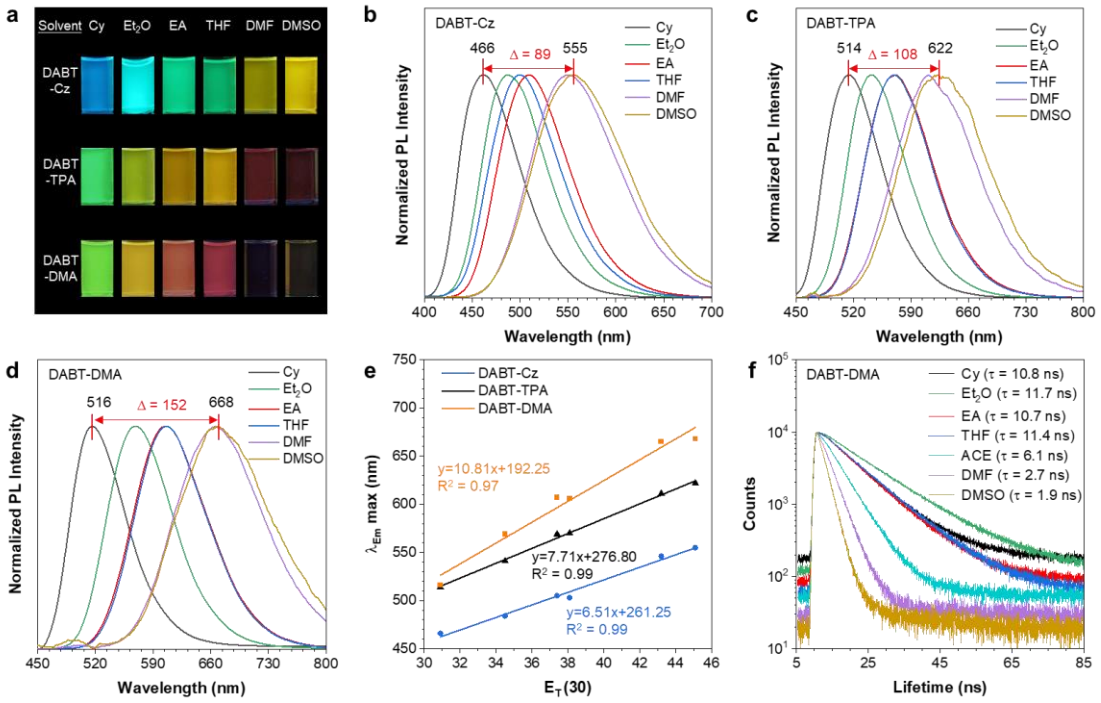

Figure 3. (a) Fluorescence photographs of DABT-Cz, DABT-TPA, and DABT-DMA in solvents with different polarities taken under a 365 nm UV irradiation. (b-d) Normalized PL spectra of DABT-Cz (b), DABT-TPA (c), and DABT-DMA (d) in different organic solvents. The absorption maximum of each solution was chosen as its excitation wavelength. Concentration: 10 μM. Δ represents the wavelength in DMSO minus the wavelength in Cy. (e) The linear relationship between the maximum emission wavelength and the solvent's polarity of DABT-Cz, DABT-TPA, and DABT-DMA. (f) PL decay curves and lifetimes (τ) of DABT-DMA in different organic solvents. Concentration: 10 μM.

Lipid droplets-targeted imaging

The polarity-dependent properties of the DABT-series molecules enable them to serve as probes for monitoring polarity changes in organelles. To ensure the potential application in biological imaging, 3-[4,5-dimethylthiazol-2-yl]-2,5-diphenyl-tetrazolium bromide (MTT) assay has been used to evaluate the cytotoxicity in different cells. Compared to DABT-Cz and DABT-TPA, DABT-DMA exhibits the lowest cytotoxicity with the SH-SY5Y cell survival rate still over 95% even at a concentration up to 50 μM (Figures 4a and S14). More significantly, the cell viability comparison between DABT-DMA and its control molecule BT-DMA without the natural alicycle skeleton undoubtedly confirms the superior biocompatibility of DABT-DMA over the "non-natural" control compound (Figure 4a). Similar results have been observed in HFL1 cells, re-confirming the outstanding biocompatible of DABT-DMA (Figure S15). The above MTT data demonstrate the best biocompatibility of the nature-inspired DABT-DMA to be applied in biological experiments. Additionally, the subcellular co-localization of DABT-DMA co-incubated with commercial dyes of Lipidtox Deep Red (LIPDR), LysoTracker® Deep Red FM (LTDR), and MitoTracker® Green FM (MTG) in cell imaging has been studied. As shown in Figure 4b, Pearson's correlation coefficient (R^2) of 0.91 for the co-localization of DABT-DMA with LIPDR indicates that DABT-DMA can specifically target LDs. In contrast, the ability of DABT-DMA to target lysosomes and mitochondria is relatively weak, with R^2 of 0.74 and 0.58,

respectively. Furthermore, both DABT-Cz and DABT-TPA have been applied in LDs co-localization with respective R^2 of 0.75 and 0.61 (Figure S16), again proving the best LDs imaging capability of DABT-DMA. The above-mentioned cell imaging results indicate that DABT-DMA in the DABT-series molecules exhibits the most promising LDs imaging capability due to its lowest cytotoxicity and best targeting ability.

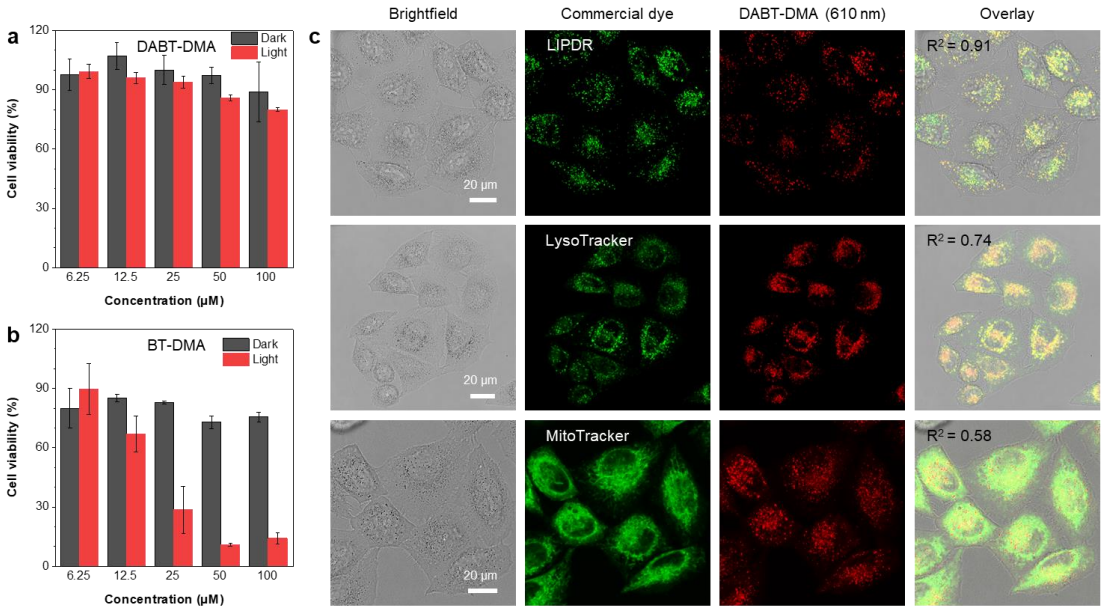

Figure 4. (a-b) The viability of SH-SY5Y cells following exposure to specified concentrations of DABT-DMA (a) and BT-DMA (b), under conditions with and without light irradiation. (c) Co-localization of DABT-DMA (10 μM, 2 h) in HeLa cells after coincubated with LIPDR (200 nM, 15 min), LTDR (200 nM, 15 min) or MTG (200 nM, 15 min). DABT-DMA: λ_{ex} = 405 nm; λ_{em} = 590 ± 20 nm. LIPDR: λ_{ex} = 640 nm; λ_{em} = 680 ± 20 nm. LTDR: λ_{ex} = 633 nm; λ_{em} = 720± 20 nm. MTG: λ_{ex} = 488 nm; λ_{em} = 510 ± 20 nm. Scale bars: 20.0 μm.

Imaging of the lipid evolution during Alzheimer's disease associated with neurodegenerative processes

Lipid metabolism is closely related to AD[55-56], yet probes to detect polarity and composition change of lipids in LDs during AD have not been reported. Given the excellent polarity dependence and biocompatibility of DABT-DMA in LDs imaging, a confocal laser scanning microscopy imaging of LIPDR and DABT-DMA has been carried out (Figure 5). The brightfield channel indicates the continuous morphological

change of SH-SY5Y cells during the amyloid-β induced AD process of 24 days. LIPDR channel records the distribution of LDs during the AD process. Given the polarity-responsive emission of DABT-DMA, the red and blue channels at 610 and 550 nm can be assigned for the high polar and low polar substances, respectively (vide supra). Hence, DABT-DMA can be utilized to monitor the polarity changes in LDs during the AD process. During this process, the imaging intensity of the red channel remains almost unchanged, suggesting that no significant change in the high polar components inside the LDs can be observed. In contrast, the increasing fluorescence intensity in the blue channel indicates the gradual generation and accumulation of low polar components within LDs. It is inspiring that the overlay of the LIPDR and the DABT-DMA (550 nm) channels changes during the AD process from a major green doped with little cyan fluorescence to a main cyan doped with scare blue emission. This complex and substantial change indicates that the newly generated low polar component is indeed produced within the LDs, which can be confirmed by the co-localization of DABT-DMA (550 nm) and LIPDR to generate cyan fluorescence. However, prolonged AD treatment can lead to the release of a portion of substances with low polarity from LDs to the cytoplasm, hence exhibiting blue fluorescence in the overlay. This may be related to changes in permeability caused by the LD damage[57-58]. Moreover, the polarity response of DABT-DMA is accompanied by changes in fluorescence lifetime in addition to wavelength variation. Therefore, FLIM has been used to monitor changes in the LD polarity (Figure 5). The experimental results show that the average fluorescence lifetime increases from 3.5 to 5.8 ns, indicating a continuous increase of low polar lipids during AD (vide supra), which is consistent with the co-localization imaging results. No doubt, DABT-DMA can be applied as a polarity-dependent bio-sensor with a dual responsiveness of distinct fluorescence wavelength and lifetime. This further confirms that the AD process can cause polarity change in LDs, with the low polar components continuously increased and partially freed outside the LDs.

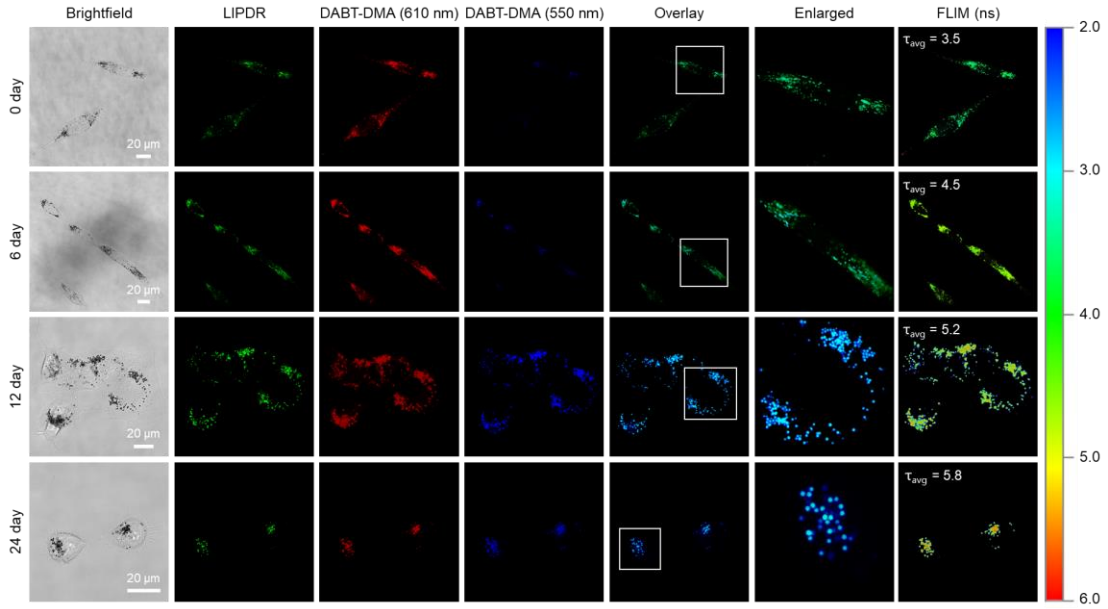

Figure 5. Monitoring the variation of lipid droplet polarity during the neurodegenerative progression in AD within SH-SY5Y cells by fluorescent imaging and FLIM during the AD process using DABT-DMA (10 μM). The amyloid-β induced AD of SH-SY5Y cells was incubated with DABT-DMA (10 μM) for 12 h. Then, the cells were incubated with LIPDR (200 nM) for 15 min before imaging using confocal microscopy. DABT-DMA: λ_{ex} = 405 nm; λ_{em} = 550 ± 20 nm and 610 ± 20 nm. LIPDR: λ_{ex} = 640 nm; λ_{em} = 680 ± 20 nm. Scale bars: 20 μm.

Structural investigation on the increased low polar substances in LDs

To further investigate the composition of the newly generated low polar components in the neurodegenerative progression, the cholesterol co-localization commercial dye of BODIPY-Cholesterol has been applied in the imaging studies together with the steroid-like structure of DABT-DMA. The extremely high R^2 of DABT-DMA with BODIPY-Cholesterol (0.94) indicates that DABT-DMA can be used to image the distribution of cholesterol analogs within LDs (Figure S17). Again, in the neurodegenerative progression, an increase of low polar components can be observed (Figure 6). Further investigation into the overlay of BODIPY-Cholesterol, DABT-DMA (610 nm), and DABT-DMA (550 nm) reveal that both the high polarity components (red channel) and the low polarity components (blue channel) are well colocalized with BODIPY-Cholesterol. This suggests that the increased low polar substances in the 550

nm channel exhibit a cholesterol-like structure. The above-mentioned results clearly indicate that a single probe of DABT-DMA can preliminarily verify the cholesterol-like structure of the generated low polar lipids in LDs during the AD process, in combination with the dual imaging capabilities of commercial probes of LIPDR (LDs imaging) and BODIPY-Cholesterol (cholesterol imaging). Given the strong link between disrupted lipid metabolism and AD[56, 59], this study proposes that the Aβ protein could induce dysfunction of lipid droplets, which in turn results in the accumulation of cholesterol analogs, further exacerbating the pathological features of AD.

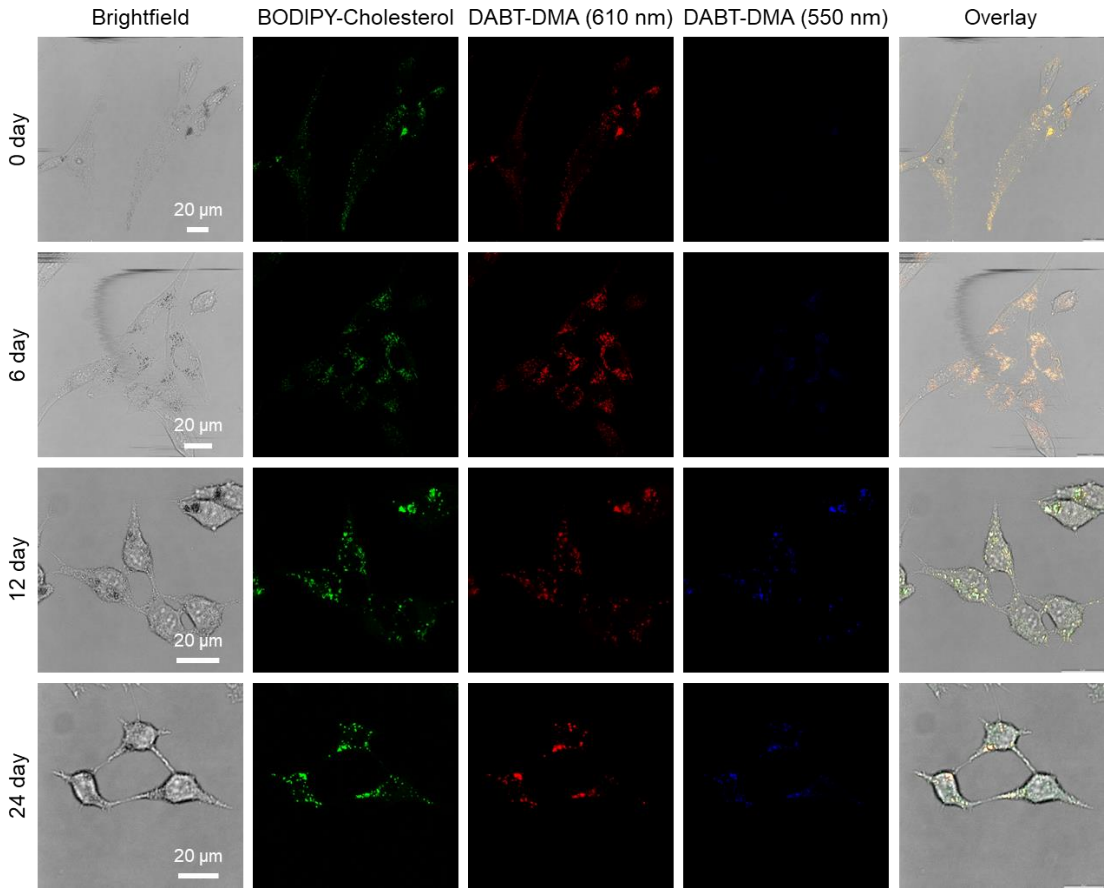

Figure 6. Monitoring the alternations in lipids composition of lipid droplets during the neurodegenerative progression in AD within SH-SY5Y cells using DABT-DMA. The amyloid-β pretreated SH-SY5Y cells were incubated with DABT-DMA (10 μM) 12 h before the cell imaging. Then, the cells were incubated with BODIPY-Cholesterol (200 nM) for 15 min before imaging using confocal microscopy. DABT-DMA: λ_{ex} = 405 nm; λ_{em} = 550 ± 20 nm and λ_{em} = 610 ± 20 nm. BODIPY-Cholesterol: λ_{ex} = 505 nm; λ_{em} = 530 ± 20 nm. Scale bars: 20.0 μm.

Conclusion

To the best of our knowledge, the exploration of polarity-dependent sensors with electron acceptors of variable structures has attracted intensive interest in the past. Unfortunately, most of the reported ones are originated from petrochemicals with finite structural variations. Herein, a nature-inspired electron acceptor (DABT) with a unique steroid-like structure has been designed from natural rosin. With electron donors from Cz to DMA, red-shifted and strengthened emission can be synchronically achieved in addition to the TICT effect. Further, the steroid-like natural electron acceptor brings both advantageous biocompatibility and targeting capability in the DMA-substituted compound DABT-DMA, resulting in its sensing ability in LDs with dual responsiveness of both distinct fluorescence wavelength and lifetime due to its strongest solvent effect. More importantly, DABT-DMA can for the first time verify that the Aβ protein-induced AD goes through LDs polarity variation, which is attributed to the production and accumulation of cholesterol analogs in LDs. This work not only proposes a novel natural skeleton-derived electron acceptor with a steroid-like structure that brings both biocompatibility and targeting ability but also applies it in visualizing the lipid evolution in LDs during AD, offering a fresh understanding in pathophysiological mechanisms for AD.

Associated Content

Supporting Information

The Supporting Information is available free of charge.

Experimental details, NMR, HRMS, and additional photophysical data (PDF)

Accession Codes

Deposition Number 2408038 (DABT-TPA) and 2408039 (DABT-DMA) contain the supplementary crystallographic data for this paper. These data can be obtained free of charge via the joint Cambridge Crystallographic Data Centre (CCDC).

Notes

The authors declare no competing financial interest.

Acknowledgments

Support from the National Natural Science Foundation of China (21601087), the Natural Science Foundation of Jiangsu Province (BK20231296), the Open Fund of Guangdong Provincial Key Laboratory of Luminescence from Molecular Aggregates, Guangzhou 510640, China (South China University of Technology (2023B1212060003)), the Shenzhen Key Laboratory of Functional Aggregate Materials (ZDSYS20211021111400001), the Science Technology Innovation Commission of Shenzhen Municipality (KQTD20210811090142053), and the Key Research and Development Project of Yunnan Province (202303AC100010). We also thank the AIE Institute (www.aietech.org.cn) for providing some AIE materials.

References

(1) Atanasov, A. G.; Waltenberger, B.; Pferschy-Wenzig, E.-M.; Linder, T.; Wawrosch, C.; Uhrin, P.; Temml, V.; Wang, L.; Schwaiger, S.; Heiss, E. H.; et al. Discovery and resupply of pharmacologically active plant-derived natural products: A review. *Biotechnol. Adv.* **2015,** *33* (8), 1582-1614.

(2) Shan, M.; Yu, S.; Yan, H.; Guo, S.; Xiao, W.; Wang, Z.; Zhang, L.; Ding, A.; Wu, Q.; Li, S. F. Y. A Review on the Phytochemistry, Pharmacology, Pharmacokinetics and Toxicology of Geniposide, a Natural Product. *Molecules* **2017,** *22* (10), 1689.

(3) Yang, Z.; Sun, X.; Jin, D.; Qiu, Y.; Chen, L.; Sun, L.; Gu, W. Novel Camphor Sulfonohydrazide and Sulfonamide Derivatives as Potential Succinate Dehydrogenase Inhibitors against Phytopathogenic Fungi/Oomycetes. *J. Agric. Food. Chem.* **2023,** *71* (1), 174-185.

(4) Atanasov, A. G.; Zotchev, S. B.; Dirsch, V. M.; Orhan, I. E.; Banach, M.; Rollinger, J. M.; Barreca, D.; Weckwerth, W.; Bauer, R.; Bayer, E. A.; et al. Natural products in drug discovery: advances and opportunities. *Nat. Rev. Drug. Discovery* **2021,** *20* (3), 200-216.

(5) Cen, P.; Huang, J.; Jin, C.; Wang, J.; Wei, Y.; Zhang, H.; Tian, M. Aggregation-induced emission luminogens for in vivo molecular imaging and theranostics in cancer. *Aggregate* **2023,** *4* (5), e352.

(6) Li, Q.; Zhang, P.; Wang, P.; Yan, C.; Wang, K.; Yang, W.; Dang, D.; Cao, L. A combination of covalent and noncovalent restricted-intramolecular-rotation strategy for supramolecular AIE-type photosensitizer toward photodynamic therapy. *Aggregate* **2024**, *5*, e676.

(7) Liu, S.; Xu, X.; Ye, J.; Wang, J.; Wang, Q.; Liu, Z.; Xu, J.; Fu, Y. Metal-coordinated nanodrugs based on natural products for cancer theranostics. *Chem. Eng. J.* **2023,** *456*, 140892.

(8) Safford, W. E. Lignum nephriticum: its history and an account of the remarkable fluorescence of its infusion. *Annu. Rep. Smithsonian Inst.* **1915**, 271-298.

(9) Zhao, Z.; Zhang, H. K.; Lam, J. W. Y.; Tang, B. Z. Aggregation-Induced Emission: New Vistas at the Aggregate Level. *Angew. Chem. Int. Ed.* **2020,** *59* (25), 9888-9907.

(10) Mantulin, W. W.; Song, P.-S. Excited states of skin-sensitizing coumarins and psoralens. Spectroscopic studies. *J. Am. Chem. Soc.* **1973,** *95* (16), 5122-5129.

(11) Janovská, M.; Kubala, M.; Šimánek, V.; Ulrichová, J. Fluorescence of sanguinarine: fundamental characteristics and analysis of interconversion between various forms. *Anal. Bioanal. Chem.* **2009,** *395* (1), 235-240.

(12) Duval, R.; Duplais, C. Fluorescent natural products as probes and tracers in biology. *Nat. Prod. Rep.* **2017,** *34* (2), 161-193.

(13) Wang, Z.; Zhang, Y.; Yin, J.; Yang, Y.; Luo, H.; Song, J.; Xu, X.; Wang, S. A Novel Camphor-Based "Turn-on" Fluorescent Probe with High Specificity and Sensitivity for Sensing Mercury(II) in Aqueous Medium and Its Bioimaging Application. *ACS Sustainable Chem. Eng.* **2020,** *8* (33), 12348-12359.

(14) Li, M.; Gao, Y.; Xu, K.; Zhang, Y.; Gong, S.; Yang, Y.; Xu, X.; Wang, Z.; Wang, S. Quantitatively analysis and detection of CN^- in three food samples by a novel nopinone-based fluorescent probe. *Food Chem.* **2022,** *379*, 132153.

(15) Zhong, W.; Lin, Y.; Zhao, Z.; Cai, X.-M.; Zhang, B. Sustainable Production of BioAIE Materials From Biomass. *ChemCatChem* **2024,** *16*, e202401510.

(16) Liang, Y.; Zhang, C.; Meng, Z.; Gong, S.; Tian, J.; Li, R.; Wang, Z.; Wang, S. A novel lysosome-targeting BODIPY-based fluorescent probe with two near-infrared channel signals for ratiometric detection of HClO and its application in diabetes mice model. *Sens. Actuators B Chem.* **2024,** *417*, 136044.

(17) Gu, Y.; Zhao, Z.; Su, H.; Zhang, P.; Liu, J.; Niu, G.; Li, S.; Wang, Z.; Kwok, R. T. K.; Ni, X.-L.; et al. Exploration of biocompatible AIEgens from natural resources. *Chem. Sci.* **2018,** *9* (31), 6497-6502.

(18) He, T.; Niu, N.; Chen, Z.; Li, S.; Liu, S.; Li, J. Novel Quercetin Aggregation-Induced Emission Luminogen (AIEgen) with Excited-State Intramolecular Proton Transfer for In Vivo Bioimaging. *Adv. Funct. Mater.* **2018,** *28* (11), 1706196.

(19) Lee, M. M. S.; Wu, Q.; Chau, J. H. C.; Xu, W.; Yu, E. Y.; Kwok, R. T. K.; Lam, J. W. Y.; Wang, D.; Tang, B. Z. Leveraging bacterial survival mechanism for targeting and photodynamic inactivation of bacterial biofilms with red natural AIEgen. *Cell Rep. Phys. Sci.* **2022,** *3* (3), 100803.

(20) Chen, S. S.; Wang, H.; Wu, B.; Li, Q.; Gong, J.; Zhao, Y. L.; Zhao, Y.; Xiao, X.; Lam, J. W. Y.; Zhao, Z.; et al. Natural Coumarin Isomers with Dramatically Different AIE Properties: Mechanism and Application. *ACS Cent Sci.* **2023,** *9* (5), 883-891.

(21) Cai, X.-M.; Lin, Y.; Zhang, J.; Li, Y.; Tang, Z.; Zhang, X.; Jia, Y.; Wang, W.; Huang, S.; Alam, P.; et al. Chromene-based BioAIEgens: 'in-water' synthesis, regiostructure-dependent fluorescence and ER-specific imaging. *Natl. Sci. Rev.* **2023,** *10* (11), nwad233.

(22) Cai, X.-M.; Li, S.; Wang, W.-J.; Lin, Y.; Zhong, W.; Yang, Y.; Kühn, F. E.; Li, Y.; Zhao, Z.; Tang, B. Z. Natural Acceptor of Coumarin-Isomerized Red-Emissive BioAIEgen for Monitoring Cu^{2+} Concentration in Live Cells via FLIM. *Adv. Sci.* **2024,** *11* (9), 2307078.

(23) Li, A. L.; Wang, Z.-L.; Wang, W.-Y.; Liu, Q.-S.; Sun, Y.; Wang, S.-F.; Gu, W. A novel dehydroabietic acid-based fluorescent probe for detection of Fe^{3+} and Hg^{2+} ions and its application in live-cell imaging. *Microchem. J.* **2021,** *160*, 105682.

(24) Cai, X.-M.; Lin, Y.; Li, Y.; Chen, X.; Wang, Z.; Zhao, X.; Huang, S.; Zhao, Z.; Tang, B. Z. BioAIEgens derived from rosin: how does molecular motion affect their

photophysical processes in solid state? *Nat. Commun.* **2021,** *12* (1), 1773.

(25) Sun, L.; Chen, L.; Yang, Z.; Sun, X.; Jin, D.; Qiu, Y.; Gu, W. A novel ratiometric dehydroabietic acid-based fluorescent probe for detecting HPO_4^{2-} and its application in food samples. *J. Food Compos. Anal.* **2023,** *120*, 105316.

(26) Liao, L.; Li, S.; Ke, Z.; Wang, X.; Wang, S.; Rao, X. Effect of rosin based quaternary ammonium salt on mechanical, hydrophily, antibacterial of cornstarch/polydopamine film for food packaging. *Int. J. Biol. Macromol.* **2024,** *255*, 128117.

(27) Králová, J.; Popr, M.; Valečka, J.; Bartůněk, P. Sterolight as imaging tool to study sterol uptake, trafficking and efflux in living cells. *Sci. Rep.* **2022,** *12* (1), 6264.

(28) Dumesnil, C.; Vanharanta, L.; Prasanna, X.; Omrane, M.; Carpentier, M.; Bhapkar, A.; Enkavi, G.; Salo, V. T.; Vattulainen, I.; Ikonen, E.; et al. Cholesterol esters form supercooled lipid droplets whose nucleation is facilitated by triacylglycerols. *Nat. Commun.* **2023,** *14* (1), 915.

(29) Olzmann, J. A.; Carvalho, P. Dynamics and functions of lipid droplets. *Nat. Rev. Mol. Cell Biol.* **2019,** *20* (3), 137-155.

(30) Zhao, Y.; Hu, D.; Wang, R.; Sun, X.; Ropelewski, P.; Hubler, Z.; Lundberg, K.; Wang, Q.; Adams, D. J.; Xu, R.; et al. ATAD3A oligomerization promotes neuropathology and cognitive deficits in Alzheimer's disease models. *Nat. Commun.* **2022,** *13* (1), 1121.

(31) Castañer, O.; Pintó, X.; Subirana, I.; Amor, A. J.; Ros, E.; Hernáez, Á.; Martínez-González, M. Á.; Corella, D.; Salas-Salvadó, J.; Estruch, R.; et al. Remnant Cholesterol, Not LDL Cholesterol, Is Associated With Incident Cardiovascular Disease. *J. Am. Coll. Cardiol* . **2020,** *76* (23), 2712-2724.

(32) Yvan-Charvet, L.; Bonacina, F.; Guinamard, R. R.; Norata, G. D. Immunometabolic function of cholesterol in cardiovascular disease and beyond. *Cardiovasc. Res.* **2019,** *115* (9), 1393-1407.

(33) Heneka, M. T.; van der Flier, W. M.; Jessen, F.; Hoozemanns, J.; Thal, D. R.; Boche, D.; Brosseron, F.; Teunissen, C.; Zetterberg, H.; Jacobs, A. H.; et al. Neuroinflammation in Alzheimer disease. *Nat. Rev. Immunol.* **2024**, 10.1038/s41577-024-01104-7.

(34) Qian, C.; Chen, J.; Wang, C.; Wang, Q.; Wang, X.; Wang, X. Light-controlled molecular tweezers capture specific amyloid oligomers. *Aggregate* **2023,** *5* (2), e463.

(35) Xu, Q.; Ma, Y.; Sun, Y.; Li, D.; Zhang, X.; Liu, C. Protein amyloid aggregate: Structure and function. *Aggregate* **2023,** *4* (4), e333.

(36) Varma, V. R.; Büşra Lüleci, H.; Oommen, A. M.; Varma, S.; Blackshear, C. T.; Griswold, M. E.; An, Y.; Roberts, J. A.; O'Brien, R.; Pletnikova, O.; et al. Abnormal brain cholesterol homeostasis in Alzheimer's disease—a targeted metabolomic and transcriptomic study. *npj Aging Mech. Dis.* **2021,** *7* (1), 11.

(37) Xue-shan, Z.; juan, P.; Qi, W.; Zhong, R.; Li-hong, P.; Zhi-han, T.; Zhi-sheng, J.; Gui-xue, W.; Lu-shan, L. Imbalanced cholesterol metabolism in Alzheimer's disease. *Clin. Chim. Acta* **2016,** *456*, 107-114.

(38) Wang, H.; Kulas, J. A.; Wang, C.; Holtzman, D. M.; Ferris, H. A.; Hansen, S. B. Regulation of beta-amyloid production in neurons by cholesterol. *Proc. Natl. Acad. Sci. U. S. A.* **2021,** *118* (33), 12.

(39) Zheng, Z.; Yang, Y.; Wang, P.; Gou, X.; Gong, J.; Wu, X.; Bao, Z.; Liu, L.; Zhang, J.; Zou, H.; et al. A Bright Two-Photon Lipid Droplets Probe with Viscosity-Enhanced Solvatochromic Emission for Visualizing Lipid Metabolic Disorders in Deep Tissues. *Adv. Funct. Mater.* **2023,** *33* (35), 2303627.

(40) Ma, J.; Sun, R.; Xia, K.; Xia, Q.; Liu, Y.; Zhang, X. Design and Application of Fluorescent Probes to Detect Cellular Physical Microenvironments. *Chem. Rev.* **2024,** *124* (4), 1738-1861.

(41) Sha, J.; Liu, W.; Zheng, X.; Guo, Y.; Li, X.; Ren, H.; Qin, Y.; Wu, J.; Zhang, W.; Lee, C.-S.; et al. Polarity-Sensitive Probe for Two-Photon Fluorescence Lifetime Imaging of Lipid Droplets In Vitro and In Vivo. *Anal. Chem.* **2023,** *95* (41), 15350-15356.

(42) Yang, W. C.; Li, S. Y.; Ni, S.; Liu, G. Advances in FRET-based biosensors from donor-acceptor design to applications. *Aggregate* **2023,** *5* (2), e460.

(43) Xu, S.; Duan, Y.; Liu, B. Precise Molecular Design for High-Performance Luminogens with Aggregation-Induced Emission. *Adv. Mater.* **2019,** *32* (1), 1903530.

(44) Lei, Z.; Zhang, F. Molecular Engineering of NIR-II Fluorophores for Improved

Biomedical Detection. *Angew. Chem. Int. Ed.* **2021,** *60* (30), 16294-16308.

(45) Rout, Y.; Montanari, C.; Pasciucco, E.; Misra, R.; Carlotti, B. Tuning the Fluorescence and the Intramolecular Charge Transfer of Phenothiazine Dipolar and Quadrupolar Derivatives by Oxygen Functionalization. *J. Am. Chem. Soc.* **2021,** *143* (26), 9933-9943.

(46) Cansu-Ergun, E. G. Chemical Insight Into Benzimidazole Containing Donor-Acceptor-Donor Type Π-Conjugated Polymers: Benzimidazole As An Acceptor. *Polym. Rev.* **2017,** *58* (1), 42-62.

(47) Yang, S.; Zhang, J.; Zhang, Z.; Zhang, R.; Ou, X.; Xu, W.; Kang, M.; Li, X.; Yan, D.; Kwok, R. T. K.; et al. More Is Better: Dual-Acceptor Engineering for Constructing Second Near-Infrared Aggregation-Induced Emission Luminogens to Boost Multimodal Phototheranostics. *J. Am. Chem. Soc.* **2023,** *145* (41), 22776-22787.

(48) Yang, S.; Jia, Q.; Ou, X.; Sun, F.; Song, C.; Zhao, T.; Kwok, R. T. K.; Sun, J.; Zhao, Z.; Jacky W. Y. Lam; et al. Integration of Motion and Stillness: A Paradigm Shift in Constructing Nearly Planar NIR-II AlEgen with Ultrahigh Molar Absorptivity and Photothermal Effect for Multimodal Phototheranostics. *J. Am. Chem. Soc.* **2025**, https://doi.org/10.1021/jacs.4c15216.

(49) Miao, T.-T.; Tao, X.-B.; Li, D.-D.; Chen, H.; Jin, X.-Y.; Geng, Y.; Wang, S.-F.; Gu, W. Synthesis and biological evaluation of 2-aryl-benzimidazole derivatives of dehydroabietic acid as novel tubulin polymerization inhibitors. *RSC Adv.* **2018,** *8* (31), 17511-17526.

(50) Zhou, L.; Chen, J. X.; Ji, S. M.; Chen, W. C.; Huo, Y. P. Research Progress of Red Thermally Activated Delayed Fluorescent Materials Based on Quinoxaline. *Acta Chim. Sinica* **2022,** *80* (3), 359-372.

(51) Ojha, M.; Banerjee, M.; Mandal, M.; Singha, T.; Ray, S.; Datta, P. K.; Mandal, M.; Anoop, A.; Singh, N. D. P. Two-Photon-Responsive "TICT + AIE" Active Naphthyridine-BF_2 Photoremovable Protecting Group: Application for Specific Staining and Killing of Cancer Cells. *ACS Appl. Mater. Interfaces* **2024,** *16* (17), 21486-21497.

(52) Zhang, J.; Tu, Y.; Shen, H.; Lam, J. W. Y.; Sun, J.; Zhang, H.; Tang, B. Z.

Regulating the proximity effect of heterocycle-containing AIEgens. *Nat. Commun.* **2023,** *14* (1), 3772.

(53)53. Lee, Will W. H.; Zhao, Z.; Cai, Y.; Xu, Z.; Yu, Y.; Xiong, Y.; Kwok, R. T. K.; Chen, Y.; Leung, N. L. C.; Ma, D.; et al. Facile access to deep red/near-infrared emissive AIEgens for efficient non-doped OLEDs. *Chem. Sci.* **2018,** *9* (28), 6118-6125.

(54)Yu, Y.; Xing, H.; Liu, D.; Zhao, M.; Sung, H. H. Y.; Williams, I. D.; Lam, J. W. Y.; Xie, G.; Zhao, Z.; Tang, B. Z. Solution-processed AIEgen NIR OLEDs with EQE Approaching 15 %. *Angew. Chem. Int. Ed.* **2022,** *61* (26), e202204279.

(55)Yoon, J. H.; Seo, Y.; Jo, Y. S.; Lee, S.; Cho, E.; Cazenave-Gassiot, A.; Shin, Y. S.; Moon, M. H.; An, H. J.; Wenk, M. R.; et al. Brain lipidomics: From functional landscape to clinical significance. *Sci. Adv.* **2022,** *8* (37), eadc9317.

(56)Prakash, P.; Manchanda, P.; Paouri, E.; Bisht, K.; Sharma, K.; Wijewardhane, P. R.; Randolph, C. E.; Clark, M. G.; Fine, J.; Thayer, E. A.; et al. Amyloid β Induces Lipid Droplet-Mediated Microglial Dysfunction in Alzheimer's Disease. *bioRxiv* **2024**, 2023.06.04.543525.

(57)Haney, M. S.; Pálovics, R.; Munson, C. N.; Long, C.; Johansson, P. K.; Yip, O.; Dong, W.; Rawat, E.; West, E.; Schlachetzki, J. C. M.; et al. APOE4/4 is linked to damaging lipid droplets in Alzheimer's disease microglia. *Nature* **2024,** *628* (8006), 154-161.

(58)Kao, Y.-C.; Ho, P.-C.; Tu, Y.-K.; Jou, I. M.; Tsai, K.-J. Lipids and Alzheimer's Disease. *Int. J. Mol. Sci.* **2020,** *21* (4), 1505.

(59)Habchi, J.; Chia, S.; Galvagnion, C.; Michaels, T. C. T.; Bellaiche, M. M. J.; Ruggeri, F. S.; Sanguanini, M.; Idini, I.; Kumita, J. R.; Sparr, E.; et al. Cholesterol catalyses Aβ42 aggregation through a heterogeneous nucleation pathway in the presence of lipid membranes. *Nat. Chem.* **2018,** *10* (6), 673-683.

Table of Contents